



Cite this: *RSC Adv.*, 2020, **10**, 26804

Received 22nd April 2020  
 Accepted 30th June 2020

DOI: 10.1039/d0ra03599h

[rsc.li/rsc-advances](http://rsc.li/rsc-advances)

## 2D BeP<sub>2</sub> monolayer: investigation of electronic and optical properties by driven modulated strain

Shivam Kansara, \*<sup>a</sup> Yogesh Sonvane, \*<sup>b</sup> P. N. Gajjar <sup>c</sup> and Sanjeev K. Gupta <sup>ad</sup>

Recently, the two-dimensional (2D) material beryllium diphosphide (BeP<sub>2</sub>) has attracted significant attention for potential device applications due to its Dirac semimetal state, dynamic and thermal stability, and high carrier mobility. In this work, we investigated its electronic and optical properties under biaxial Lagrangian strain using density functional theory (DFT). Electronic band gaps and effective charge carrier mass were highly sensitive to the Lagrangian strain of BeP<sub>2</sub> monolayer. The bandgaps of BeP<sub>2</sub> varied from 0 eV to 0.30 eV for 2% to 8% strain, where the strain range is based on the final stable condition of the system. The absorption spectra for the dielectric properties show the highest absorption peaks in the infrared (IR) region. These abundant strain-dependent studies of the BeP<sub>2</sub> monolayer provide guidelines for its application in infrared sensors and devices.

### Introduction

Strain effects in systems (metal, semiconductor, and insulator) are considered to be highly sensitive effective and convenient tools for their tuning electronic, transport, and optical properties.<sup>1–6</sup> The applied strain effects can be interpreted as an elastic field applied to materials, which modifies the geometrical structure of their crystals due to the interaction between the elastic field and crystalline field, thus influencing the electronic band structure,<sup>7</sup> and finally tuning the physical,<sup>8</sup> chemical and catalytic properties<sup>9</sup> of materials. These tools are especially reasonable for the design of two-dimensional (2D) crystals because their low-dimensional structure can sustain much larger strain compared to bulk crystals.<sup>10,11</sup> For example, the black phosphorus (BP) monolayer has been strained up to a noteworthy value of 30% without any dislocation or plastic deformation in its crystal structure,<sup>12</sup> giving a wide range to tune its mechanical and electronic properties.<sup>1</sup> Besides, as a universal structure, the 2D BeP<sub>2</sub> material with Dirac cones found precisely at the Fermi level,<sup>13</sup> high carrier mobility and novel strain-tunable Dirac semimetal state of ultrathin BeP<sub>2</sub> can also be altered by strain.

Beryllium di-phosphide (BeP<sub>2</sub>) has attracted significant attention recently due to its Dirac semimetal state, excellent stability in the ambient environment, thermal stability, and high carrier mobility. Herein, we concentrated on a P and Be

atomic sheet because Be is generally utilized as one of the constituent components in 2D binary compounds, including h-BeS,<sup>14</sup> Be<sub>2</sub>C,<sup>15</sup> and Be<sub>5</sub>C<sub>2</sub>.<sup>16</sup> Besides, a BeN<sub>2</sub> nanosheet is considered to be stable with outstanding properties due to its high stability and direct bandgap.<sup>13,17</sup> Dirac semimetals are incredible directors of power, even though they have zero band gaps, and thus cannot be turned off. Due to the specific limitation of topology insulators in photonic devices,<sup>18,19</sup> we applied Lagrangian strain to the BeP<sub>2</sub> monolayer for bandgap opening. To date, there are no reports on engineering the physical and corresponding anisotropic properties of BeP<sub>2</sub>, and thus the present work focused on the examination of its in-plane anisotropic properties, including its stable structural, electrical, optical and anisotropies.

Nowadays, various researchers have focused on Dirac semimetal materials due to their rapid charge transport and significantly high carrier mobility.<sup>20–25</sup> There are numerous reports on tuning the electronic properties of Dirac semimetal, semiconductor, and insulator monolayers for functional devices.<sup>20,23,26–36</sup> Wang *et al.*<sup>26,27</sup> reported a tunable 1T-WTe<sub>2</sub> monolayer semimetal having a small bandgap by ambipolar conduction. Yu *et al.*<sup>29</sup> reported tuning the bandgap of bilayer graphene *via* molecular doping with benzyl viologen molecules. Semi-metallic single-layer buckled silicene and germanene were transformed into an open bandgap using an external electric field.<sup>31</sup> Mu *et al.* reported a metallic to semi-metal transition with a Dirac point in BeB<sub>2</sub> monolayer *via* 5% isotropic compression, while it became metallic again under a larger compression.<sup>20</sup>

In this work, the effects of strain on monolayer BeP<sub>2</sub> were investigated using first-principles calculations. We investigated the change in the electronic and optical properties of the BeP<sub>2</sub> monolayer under Lagrangian strain. Bandgap engineering

<sup>a</sup>Department of Physics, SMMPISR, Kadi Sarva Vishwavidyalaya, Gandhinagar 382015, India. E-mail: shivam\_msc@ldrp.ac.in

<sup>b</sup>Advanced Materials Lab, Department of Applied Physics, S.V. National Institute of Technology, Surat 395007, India. E-mail: yas@phy.svit.ac.in

<sup>c</sup>Department of Physics, Gujarat University, Ahmedabad 380009, India

<sup>d</sup>Computational Materials and Nanoscience Group, Department of Physics, St. Xavier's College, Ahmedabad 380009, India. E-mail: sanjeev.gupta@sxca.edu.in



using strain is an effective method and has been used in other 2D thin films. Besides, the strain effects on the effective mass of electrons and holes were deliberately explored.

## Methodology

We have carried out *ab initio* DFT calculations, which were implemented using the Vienna *Ab initio* Simulation Package (VASP).<sup>37,38</sup> The projector augmented wave (PAW)<sup>39</sup> pseudopotential with the Perdew–Burke–Ernzerhof (PBE) exchange–correlation function was exploited to study the electronic properties of the semiconductor BeP<sub>2</sub> monolayer. An orthorhombic unit cell was adopted for the planer global structure (shown in Fig. 1). Here, a vacuum spacing of greater than 16 Å was employed to prevent mirror interactions with the imaginary system in the direction perpendicular (z-axis) to the nanosheet. For the plane-wave basis set, we considered a kinetic energy cut-off of 500 eV. All structures were fully relaxed up to ionic forces less than 0.001 eV Å<sup>-1</sup> for each atom using the conjugate gradient method from the Hellmann–Feynman theorem. The Brillouin zone (BZ) integrations were sampled using 10 × 10 × 1 and 12 × 12 × 1 special *k*-point sampling in the Monkhorst–Pack scheme<sup>40</sup> for the geometry optimizations, and electronic and optical properties, respectively. The convergence criteria for the energy cut-off, *k*-point mesh, and smearing width were performed to reach an accuracy of total energy error less than 0.001 eV per cell. To investigate the strain effects on the atomic configuration and the electronic structure of the monolayer BeP<sub>2</sub>, we applied an external strain to the biaxial xy-axis, and allowed all atoms to freely relax. To calculate the dielectric frequency-dependent optical properties such as dielectric function, electron energy loss spectra (EELS), and reflectance and absorbance spectra, the random phase approximation (RPA) was used.<sup>41</sup>

## Results and discussion

### Structure and stability

Initially, we investigated the general structure of BeP<sub>2</sub> to understand its properties, which are usually determined by its structure, and then studied the effect of Lagrangian strain on the structure of the BeP<sub>2</sub> monolayer. As shown in Fig. 1(a), the supercell 2 × 2 of the BeP<sub>2</sub> monolayer was represented by a hexagonal shape with Be and P atoms, which is consistent with other works.<sup>13</sup> One unit cell of the BeP<sub>2</sub> monolayer (sketched green box in Fig. 1(a)) contains four Be atoms and eight P atoms, with a calculated lattice constant (displayed in Fig. 1(a)) of 9.70 Å and 6.98 Å for the x and y-direction, respectively. Fig. 1(b) shows the side phase of the BeP<sub>2</sub> monolayer. The corresponding path through the high symmetry points in the first Brillouin zone for the orthorhombic structure due to the electronic properties is shown in Fig. 1(c). Here, one Be atom forms a trigonal bond to an adjacent N with sp<sup>2</sup> hybridization and no distortion. The distance between the Be and P atoms is ~2.06 Å (varying) and P and P atoms is ~2.09 Å (varying), as shown by in Fig. 1, which is in good agreement with a previous work.<sup>13</sup> The explanation for the stability of the ideal BeP<sub>2</sub> monolayer has been reported previously based on phonon spectra.<sup>13</sup>

Fig. 2(a) presents the lattice constants along the x- and y-axis with different strain, which increased with an increase in strain. The variation lattice parameters affected the pressure, total energy, and binding energy of the system, which are responsible for the stability of the structure. Before investigating the various properties of the BeP<sub>2</sub> monolayer for its potential applications, we needed to confirm its stability and feasibility for its experimental synthesis. Thus, we calculated the cohesive energy of free and strain-dependent BeP<sub>2</sub> monolayers, as shown in Fig. 2(b). The binding energy  $E_{\text{binding}}$  can be calculated as follows:

$$E_{\text{binding}} = E_{\text{BeP}_2} - n(E_{\text{Be}} - E_{\text{P}}) \quad (1)$$

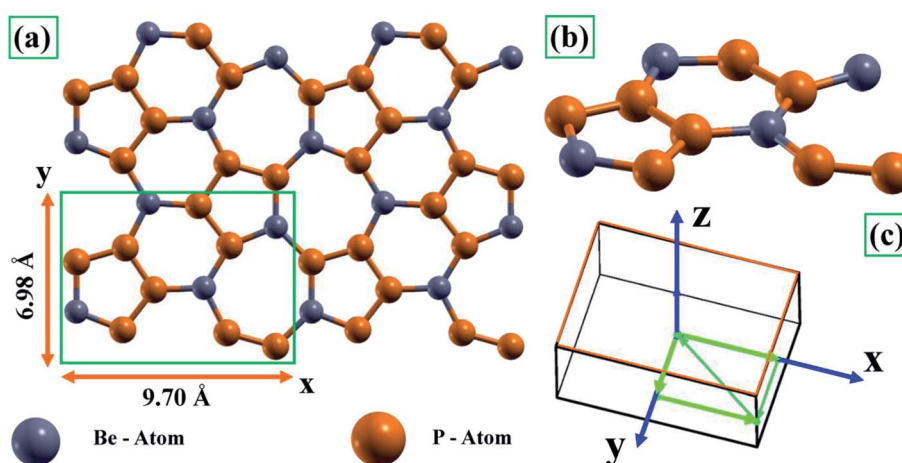


Fig. 1 (a) Top and (b) side views of BeP<sub>2</sub> monolayer. (a) The top view represents the 2 × 2 supercells of the BeP<sub>2</sub> monolayer and lattice constant of the unit cell (green box). (b) Represents the diagonal view of the BeP<sub>2</sub> monolayer (unit cell). (c) Corresponding Brillouin zone for the orthorhombic structure.



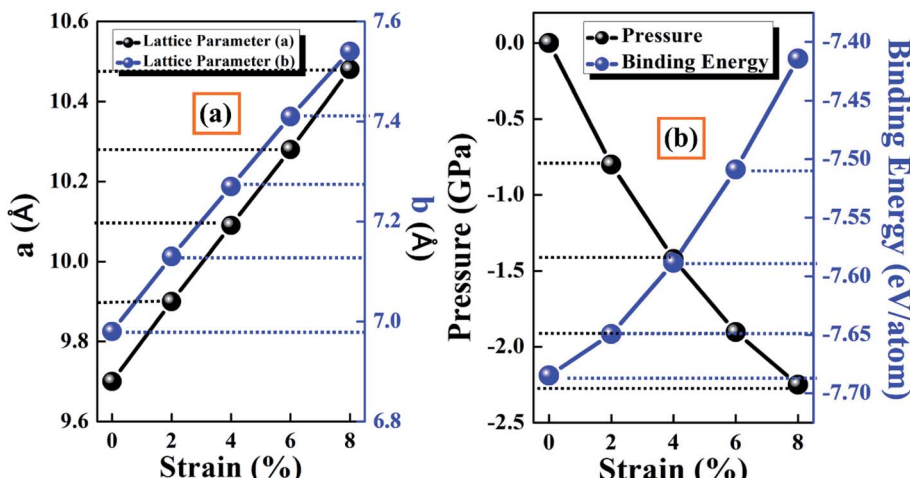


Fig. 2 Representation of (a) lattice constants (x- and y-directions) and (b) system pressure, and binding energy per atom with various Lagrangian strain.

where  $E_{\text{BeP}_2}$ ,  $E_{\text{Be}}$  and  $E_{\text{P}}$  are the total energy of the complex system, a single Be atom, and a single P atom, respectively.  $n$  is the number of atoms per unit cell. The binding energy of the  $\text{BeP}_2$  monolayer is much better compared to that of other monolayers such as graphene,<sup>42</sup> phosphorene,<sup>12</sup> carbon phosphide,<sup>43</sup>  $\text{Al}_2\text{C}$  sheet,<sup>44</sup> silicene,<sup>45</sup> and antimonene<sup>46,47</sup> of 7.62, 3.48, 5.32, 3.94, 3.55 and 4.26 eV per atom, respectively. For comparison, the cohesive energy of the  $\text{BeP}_2$  monolayer is 7.68 eV per atom, which is larger than that of available  $\text{AB}_2$ -type 2D materials such as  $\text{CaSb}_2$ ,<sup>48</sup>  $\text{BeN}_2$ ,<sup>17</sup> and  $\text{MgP}_2$ .<sup>49</sup> The high binding energy of the  $\text{BeP}_2$  monolayer of 7.68 eV per atom justifies its robust nature and relative stability. Upon applying Lagrangian strain, the cohesive energy is reduced with an increase in the pressure of the system. The previous study by Lee *et al.*<sup>50</sup> and Corsetti *et al.*<sup>51</sup> reported that systems were considered to be stable up to a pressure of  $\sim 1$  GPa for a 5 Å system, whereas in our study, we employed an  $\sim 10$  Å system, and thus the stability was sustained up to a pressure of  $\sim 2$  GPa. Thus, this proved that the system was stable under Lagrangian

strain. The reported pressure is dependent on both the confinement width and the form of the confining potential. Also, a pressure of  $\sim 1$  GPa led to a slight increase in the thermal equilibrium concentration and diffusion of vacancies, but this increase was much smaller than that of self-interstitials.

### Electronic properties

Fig. 3(a) and (b) presents the calculated band structure and partial density of states (PDOS) of a strain-free  $\text{BeP}_2$  monolayer. The curvature of the band structure of the  $\text{BeP}_2$  monolayer (Fig. 3(a)) is similar to the expected band structure of graphene, where in particular, it shows a linear Dirac-type dispersion of electrons near the  $X$  points. However, the Fermi velocity,  $v$ , of the electrons in the  $\text{BeP}_2$  monolayer is lower than that of graphene.<sup>52</sup> The PDOS, as shown in Fig. 3(b), demonstrates the contribution of the orbitals of the atoms. There is a larger orbital contribution from the p orbital of the atoms than the s orbital. However, the p orbital of the P atom has a larger contribution than the p orbital of the Be atom with zero density

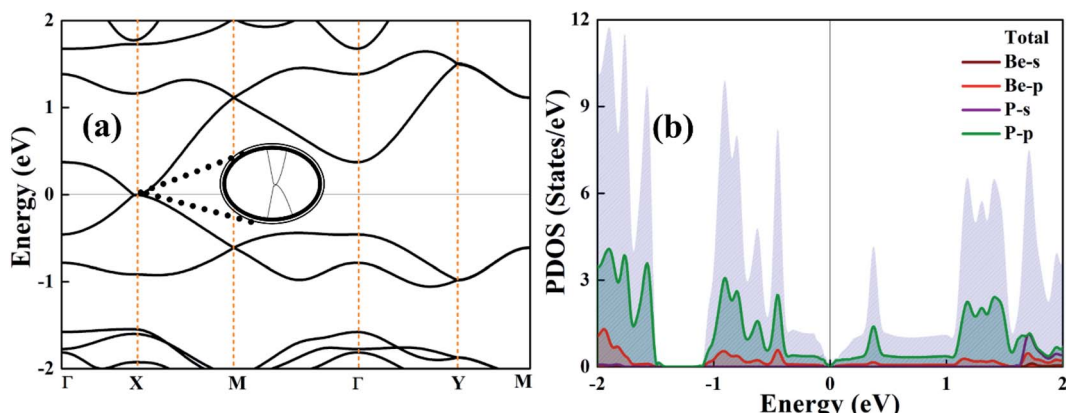


Fig. 3 (a) Electronic band structure and (b) partial density of states (PDOS) of the  $\text{BeP}_2$  monolayer. The inset figure shows the intersection of the bands.



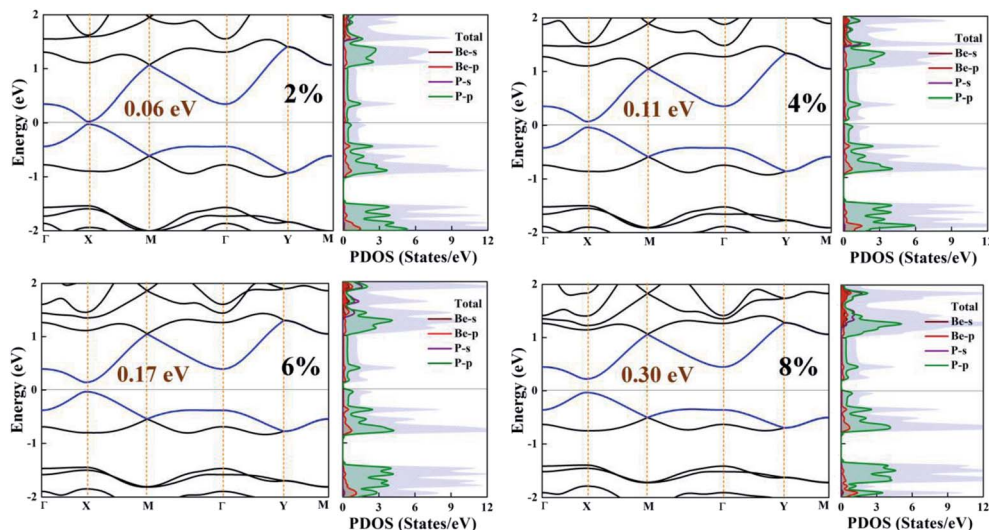


Fig. 4 Electronic band structure and partial density of states (PDOS) of the  $\text{BeP}_2$  monolayer with various Lagrangian strain.

of states (DOS) at the Fermi energy, which is responsible for the semi-metallic behavior. The presented electronic properties are in very good agreement with that previously reported by Li *et al.*<sup>13</sup> They have presented the orbital projected band structure, which can be used to evaluate the orbit correlation and is responsible for the semi-metallic behavior.

Here, the electronic band structure and PDOS of the  $\text{BeP}_2$  monolayer under Lagrangian biaxial strain is presented in Fig. 4. For biaxial strain, the strain tensor ( $e$ ) can be written as:

$$e = \begin{bmatrix} \varepsilon_{\parallel} & 0 \\ 0 & \varepsilon_{\parallel} \end{bmatrix} \quad (2)$$

where  $\varepsilon_{\parallel} = (a - a_0)/a_0$ ,  $a$  represents the lattice constant and the biaxial strain tensor ( $e$ ) is implemented in the supercells by applying the changes to the lattice parameters along the  $x$ - $y$  plane. In the biaxial strain, the varying value of  $E_X$  corresponds to the changes in strain, while there is a slight change in the values of  $E_M$  to  $E_X$ . For tensile strain,  $E_X$  increases as the strain increases, with the descending rate determined to be 60 meV per 2% strain.

The effect of strain on the band structures of the  $\text{BeP}_2$  monolayer is shown in Fig. 4, which was used to calculate the values of the effective masses (electron and hole), corresponding to the valence and conduction bands. The strain effect illustrates the major changes in the electronic band structure at the  $X$ -point. Thus, we can say that the conduction channel with the lowest energy and valence channel with the highest energy are located at the  $X$ -point. Direct band gaps appear at the  $X$ -point with an increase in strain, as shown in Fig. 4. Insight into the bonding character of the given monolayer was derived from the electronic charge density analysis, as shown in Fig. 5. It is clear that along the atomic sphere, the electrons are not limited, and their reasonable proportion resides in the interstitial region, thus the nature of the bonding is covalent for free strain systems. We calculated the partial density of states (PDOS) of the Be atoms and P atoms to understand their orbital

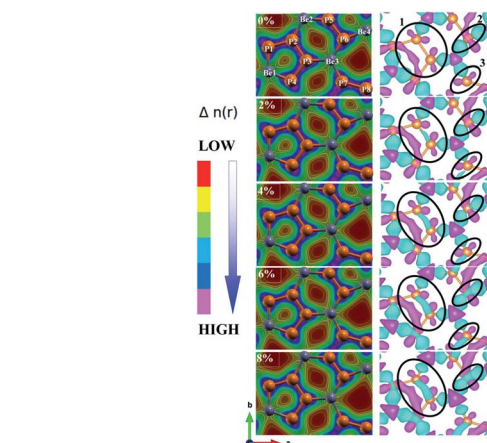


Fig. 5 Right and left side of the electronic charge contour and electron density difference of  $\text{BeP}_2$  monolayer with various Lagrangian strain.

contribution to the band structure. Here, the valence band mainly originates (larger contribution) from the 2p and 3p states of the Be and P atoms rather than the 2s and 3s states of the  $\text{BeP}_2$  monolayer.

Here, the 3p states of the P atoms form a tetrahedral contribution with the 2s states of the Be atoms. The orbital states of Be-2s and P-3p have higher orbital contributions, which are demonstrated by the higher binding energies, as shown in Fig. 2(b). The conduction and valence energy bands (*i.e.* CBE and VBE, respectively) shift toward a lower energy with Lagrangian tensile strain. Due to the Lagrangian strain, the band shift at the  $X$ -point corresponds to the bonding and delocalization character of the CBE and VBE orbitals, respectively. Thus, it can be concluded that Lagrangian tensile strain



**Table 1** The hole ( $\mu_h$ ) and electron ( $\mu_e$ ) effective mass of the  $\text{BeP}_2$  monolayer with various Lagrangian strain for the  $X$ -point of the electronic band structures

Strain (%)	0	2	4	6	8
$m_h^* (\times 10^{-3})$	—	0.61	0.75	0.93	1.15
$m_e^* (\times 10^{-3})$	—	-0.86	-0.95	-1.35	-1.44

can successfully tune the bandgap of the  $\text{BeP}_2$  monolayer for its wide application.

We calculated the effective masses of the electrons and holes for the band structure of the  $\text{BeP}_2$  monolayer using eqn (3) as follows:

$$m^* = \hbar^2 \left( \frac{d^2 \epsilon}{dk^2} \right)^{-1} \quad (3)$$

For this calculation, we used a small energy range between  $-0.2$  eV to  $+0.2$  eV for the conduction and valence bands near the  $X$ -point (bandgap), where the unit of the considered range  $\pm 0.2$  is  $2\pi/a$  ( $a$  describes the axial lattice constant). Here, the displayed band structure curve of energy *versus* K was fitted using the second-order polynomial  $\epsilon = C_1 k^2 + C_2 k + C_3$ . According to the fitting function, we obtained the curvature  $C_1 = \frac{1}{2} \times \left( \frac{d^2 \epsilon}{dk^2} \right)$ . Using the above equation and discussion, we calculated the value of the effective mass of the electrons and holes through the relation  $m^* = \hbar^2 / 2C_1$ .<sup>53</sup> The values of the effective mass of the electrons ( $m_e^*$ ) and holes ( $m_h^*$ ) are tabulated in Table 1.

The energy density represents the strength or nature of bonds. The chemical bond is a concept for realizing the properties of a structure such as stability and reactivity for host materials. The calculated charge density distribution provides significant details regarding local energy density properties.<sup>54</sup> The kinetic energy is dominant due to the positive Laplacian electron density, which is fundamental for the depletion of the bond charge. Thus, to gain deeper insight into the deformation

of the  $\text{BeP}_2$  structure under Lagrangian strain, we focused on analyzing and expressing the electronic charge contour and charge difference plots in the (110) crystallographic plane, as presented in Fig. 5. The electronic charge density contour depicts the partial ionic and strong covalent bonding of the P–P and P–Be atoms based on the Pauling electronegativity difference. The atomic bonding can be observed by the color charge scale, as displayed on the right side in Fig. 5. The color charge scale represents various colors from red to pink as low electron density to high electron density, respectively. With the approach of strain, electrons are transferred from the Be to P atoms through the closest atoms. Thus, to investigate the charge transfer between two atoms of the  $\text{BeP}_2$  monolayer, the charge density difference  $\Delta\rho$  was calculated, as illustrated in Fig. 5, using the following equation:

$$\Delta\rho = \rho_{\text{complex}} - \rho_{\text{Be}} - \rho_{\text{P}} \quad (4)$$

where  $\rho_{\text{complex}}$  is the charge density of the complex system of the  $\text{BeP}_2$  monolayer, and  $\rho_{\text{Be}}$  and  $\rho_{\text{P}}$  are the charge densities of the Be and P atoms, respectively. The cyan and pink clouds in Fig. 5 represent electron accumulation and depletion, respectively, which correspond to a gain and depletion in electronic charge, respectively. A small amount of electronic charge is depleted from the P atoms. Therefore, the black circles labeled as 1, 2 and 3 in the CDDs represent the deformation in the  $\text{BeP}_2$  structure upon the application of Lagrangian strain. Here, the charge transfer between the atoms can be observed. The charge density at points 1, 2 and 3 slowly increase with an increase in strain up to the ultimate tensile strength, *i.e.* 8% elongation. Beyond this strain, the  $\text{BeP}_2$  monolayer is observed to be a higher value than 2 GPa. Therefore, a stress–strain curve for up to 8% applied strain was observed.

## Optical properties

Here, we presented the imaginary and real part of the frequency-dependent complex dielectric function for the  $\text{BeP}_2$  monolayer under Lagrangian strain. Investigating the optical properties of the  $\text{BeP}_2$  monolayer is important for its optoelectronic applications. The electronic band structure of materials is closely

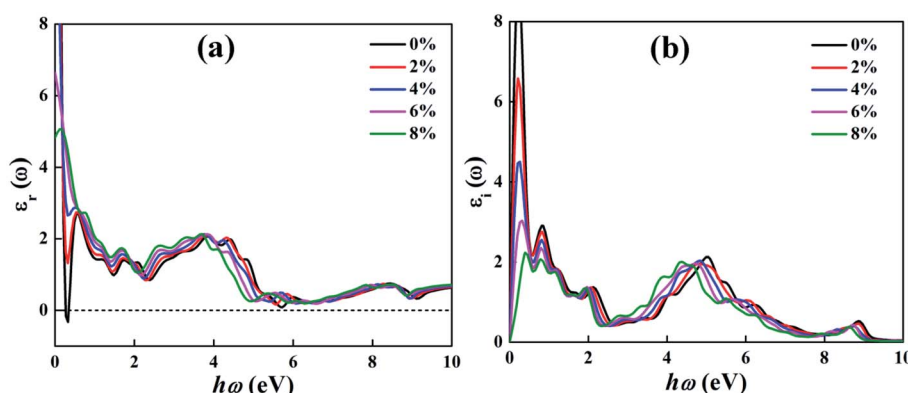


Fig. 6 Calculated optical (a) real and (b) imaginary parts of the dielectric function of the  $\text{BeP}_2$  monolayer with various Lagrangian strain.



correlated to the imaginary part  $\varepsilon_i(\omega)$ , which can be represented as shown in Fig. 6(b). The transition of the interband in  $\varepsilon_i(\omega)$  occurs from the valence band maximum (VBM) to the conduction band minimum (CBM) along the  $\Gamma$ -X direction and vicinity of the M-point of all the peaks. All the optical interband transitions are essentially due to the p orbital of the Be and P atoms, as shown by the PDOS in Fig. 3 and 4. Meanwhile, the real part  $\varepsilon_r(\omega)$  represents the electronic polarizability of the material through the Clausius–Mossotti relation. The large number of peaks for the  $\text{BeP}_2$  monolayer describe the dipole-allowed transition between states near the Van Hove singularities (VHS).<sup>55</sup> According to the literature, materials with a bandgap below 1.7 eV function outstandingly in the IR region as optical materials.<sup>56</sup>

As shown in Fig. 6(a), based on the real part of the dielectric function, we analysed the static dielectric constant at the zero frequency limits, which is 34.49, 22.37, 15.20, 6.64 and 4.82 for the 0%, 2%, 4%, 6% and 8%  $\text{BeP}_2$  monolayer, respectively, suggesting that the 0% (strain-free)  $\text{BeP}_2$  monolayer has relatively high polarizability. Also, the negative values indicate the metallic nature of the 0% (strain-free)  $\text{BeP}_2$  monolayer in the IR region. There are various peaks in the imaginary part of the dielectric function, as shown in Fig. 6(b), which is due to the electronic transitions from the 3s/3p states in the valence band to the hybridized 2p orbitals of the Be atoms and 3s/3p orbitals of the P atoms, while the last peak is due to the electronic transitions from the 2p to 3s/3p orbitals. Here, the lower and broad peaks for the dielectric properties describe the volume

plasmon oscillations and the absorption of plasmon energy, respectively. As shown in Fig. 6, it can be seen that the main loss in the optical curves occurs in the range of 8–7 eV and 8.5–9.5 eV, which is due to the oscillation of the electric dipoles and the ionizing environment.

Fig. 7(a) shows the good optical efficiency in the IR range based on the low values in the EELS curve. Fig. 7(b) and (c) present the reflectivity and absorption spectra of the  $\text{BeP}_2$  monolayer for various Lagrangian strain. Here, the interband transition can be understood based on the absorption and reflection spectra of the  $\text{BeP}_2$  monolayer, while the minimum value of the reflection and absorption is observed at 2.3 eV due to the volume plasmon oscillation from 2 to 3 eV with a gap of 1 eV. Here, the absorption coefficient was calculated as  $A(\omega) = 2\omega K(\omega)/C$ , where,  $K$  is the extinction coefficient. The maximum absorption peaks occur due to the high extinction coefficient and minimum wave transfer. According to the reflectivity in Fig. 7(b), the  $\text{BeP}_2$  monolayer is a good electromagnetic wave absorber in the absorption range of around 0 eV to 9 eV. In this absorption range, several peaks are good reflectors of UV and VIS. Table 2 presents the values of the absorption and reflection peaks and the static reflection coefficient,  $R(0)$ , based on Fig. 7(b) and (c).

By analyzing the high absorption and low EELS up to 4 eV, we can conclude that the  $\text{BeP}_2$  monolayer is an optical absorber in the IR region. The IR region has many classification names such as near IR (NIR), short-wave IR (SWIR), mid-wave IR (MWIR), and long-wave IR (LWIR) region. Due to its electric charge

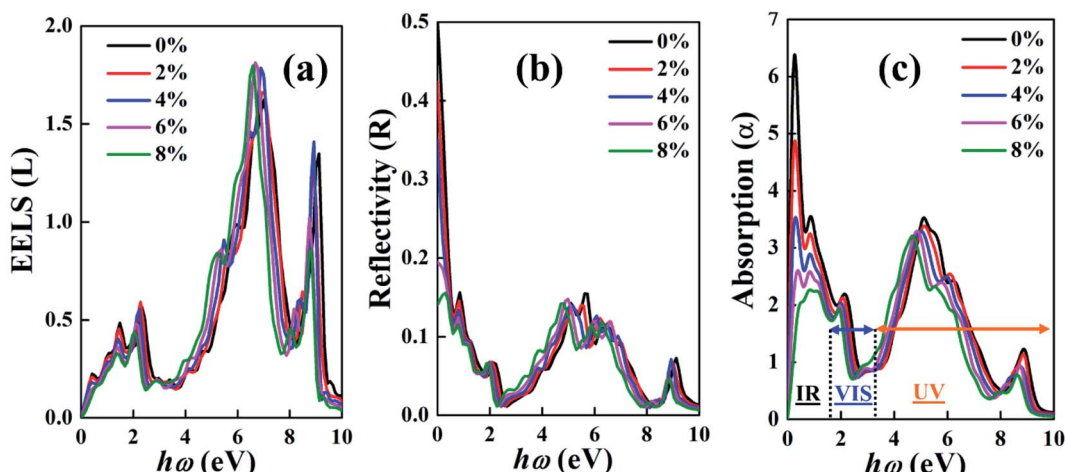


Fig. 7 Calculated (a) electron energy loss spectrum (EELS) ( $L$ ), (b) reflectivity ( $R$ ) and (c) absorption spectra ( $\alpha$ ) of the dielectric function of the  $\text{BeP}_2$  monolayer with various Lagrangian strain.

Table 2 Maximum absorption peaks of the various  $\text{BeP}_2$  monolayers with various Lagrangian strain

Strain (%)	0	2	4	6	8
Absorption peaks (eV)	2.26, 5.16, 8.81	2.17, 5.16, 8.80	2.02, 5.04, 8.72	1.98, 4.92, 8.76	1.94, 4.69, 8.61
Reflection peaks (eV)	0.86, 2.13, 5.69, 9.13	0.78, 2.10, 5.57, 8.98	0.74, 2.04, 5.08, 8.89	0.74, 2.0, 4.96, 8.89	0.74, 1.98, 4.78, 8.80
$R(0)$	0.50	0.42	0.35	0.19	0.14



oscillation and ionic behavior, the maximum reflection coefficient occurs near 5.5 eV.

## Conclusions

In conclusion, we used *ab initio* density functional theory to study the strain-dependent structural, electronic, and optical properties of the  $\text{BeP}_2$  monolayer. Accordingly, it was concluded that the stability of this system was confirmed by its cohesive energy such as 7.62, 3.48, 5.32, 3.94, 3.55 and 4.26 eV per atom and internal pressure. Upon applying tensile Lagrangian strain, the system became semiconductor in nature with direct band gaps in the range of 0.06 to 0.30 eV. Based on the dielectric function, the  $\text{BeP}_2$  nanosheets are good absorbents of electromagnetic waves in the IR region. This study is important because the bandgap is a fundamental issue that can limit the use of the emerging 2D  $\text{BeP}_2$  in the future. Thus, results present for the  $\text{BeP}_2$  nanosheets demonstrate their promising practical applications in novel mechanical-electronic devices and optical instruments such as night vision devices, thermo-graphic cameras, and infrared vibrational spectroscopy.

## Conflicts of interest

There are no conflicts to declare.

## Acknowledgements

Shivam Kansara also likes to high-performance computing clusters PARAM Shavak-C-DAC of KSV. S. K. G. would like to thank Science and Engineering Research Board (SERB), India for financial support (Grant no.: YSS/2015/001269). P. N. G. is thankful to the Department of Science and Technology, India for the support under DST-FIST and the University Grants Commission, India for the support under DRS-SAP.

## References

- 1 V. Tran, R. Soklaski, Y. Liang and L. Yang, Layer-controlled band gap and anisotropic excitons in few-layer black phosphorus, *Phys. Rev. B: Condens. Matter Mater. Phys.*, 2014, **89**, 235319.
- 2 J. Jiang, Q. Liang, S. Zhang, R. Meng, C. Tan, Q. Yang, X. Sun, H. Ye and X. Chen, Tuning the electronic and optical properties of graphane/silicane and  $\text{fBN}$ /silicane nanosheets *via* interfacial dihydrogen bonding and electrical field control, *J. Mater. Chem. C*, 2016, **4**, 8962–8972.
- 3 W. Yu, C.-Y. Niu, Z. Zhu, X. Wang and W.-B. Zhang, Atomically thin binary V–V compound semiconductor: a first-principles study, *J. Mater. Chem. C*, 2016, **4**, 6581–6587.
- 4 M. Zhang, Y. An, Y. Sun, D. Wu, X. Chen, T. Wang, G. Xu and K. Wang, The electronic transport properties of zigzag phosphorene-like MX (M = Ge/Sn, X = S/Se) nanostructures, *Phys. Chem. Chem. Phys.*, 2017, **19**, 17210–17215.
- 5 S. Kansara, S. K. Gupta and Y. Sonvane, Effect of strain engineering on 2D dichalcogenides transition metal: A DFT study, *Comput. Mater. Sci.*, 2018, **141**, 235–242.
- 6 Z. Li, X. Wang, W. Shi, X. Xing, D.-J. Xue and J.-S. Hu, Strain-engineering the electronic properties and anisotropy of  $\text{GeSe}_2$  monolayers, *RSC Adv.*, 2018, **8**, 33445–33450.
- 7 D. Çakir, H. Sahin and F. M. Peeters, Tuning of the electronic and optical properties of single-layer black phosphorus by strain, *Phys. Rev. B: Condens. Matter Mater. Phys.*, 2014, **90**, 205421.
- 8 Z. Zhang, L. Li, J. Horng, N. Z. Wang, F. Yang, Y. Yu, Y. Zhang, G. Chen, K. Watanabe and T. Taniguchi, Strain-modulated bandgap and piezo-resistive effect in black phosphorus field-effect transistors, *Nano Lett.*, 2017, **17**, 6097–6103.
- 9 H. Li, C. Tsai, A. L. Koh, L. Cai, A. W. Contryman, A. H. Fragapane, J. Zhao, H. S. Han, H. C. Manoharan and F. Abild-Pedersen, Activating and optimizing  $\text{MoS}_2$  basal planes for hydrogen evolution through the formation of strained sulphur vacancies, *Nat. Mater.*, 2016, **15**, 48.
- 10 A. S. Rodin, A. Carvalho and A. C. Neto, Strain-induced gap modification in black phosphorus, *Phys. Rev. Lett.*, 2014, **112**, 176801.
- 11 X. Peng, Q. Wei and A. Copple, Strain-engineered direct–indirect band gap transition and its mechanism in two-dimensional phosphorene, *Phys. Rev. B: Condens. Matter Mater. Phys.*, 2014, **90**, 085402.
- 12 Q. Wei and X. Peng, Superior mechanical flexibility of phosphorene and few-layer black phosphorus, *Appl. Phys. Lett.*, 2014, **104**, 251915.
- 13 X. Li and Q. Wang, Prediction of a  $\text{BeP}_2$  monolayer with a compression-induced Dirac semimetal state, *Phys. Rev. B*, 2018, **97**, 085418.
- 14 J. Yu and W. Guo, Two-dimensional hexagonal beryllium sulfide crystal, *J. Phys. Chem. Lett.*, 2013, **4**, 1856–1860.
- 15 Y. Li, Y. Liao and Z. Chen,  $\text{Be}_2\text{C}$  monolayer with quasi-planar hexacoordinate carbons: a global minimum structure, *Angew. Chem., Int. Ed.*, 2014, **53**, 7248–7252.
- 16 Y. Wang, F. Li, Y. Li and Z. Chen, Semi-metallic  $\text{Be}_5\text{C}_2$  monolayer global minimum with quasi-planar pentacoordinate carbons and negative Poisson's ratio, *Nat. Commun.*, 2016, **7**, 11488.
- 17 C. Zhang and Q. Sun, A honeycomb  $\text{BeN}_2$  sheet with a desirable direct band gap and high carrier mobility, *J. Phys. Chem. Lett.*, 2016, **7**, 2664–2670.
- 18 X. Zhang, Q. Liu, Q. Xu, X. Dai and A. Zunger, Topological insulators *versus* topological Dirac semimetals in honeycomb compounds, *J. Am. Chem. Soc.*, 2018, **140**, 13687–13694.
- 19 Z. Fedorova, C. Jörg, C. Dauer, F. Letscher, M. Fleischhauer, S. Eggert, S. Linden and G. von Freymann, Limits of topological protection under local periodic driving, *Light: Sci. Appl.*, 2019, **8**, 1–12.
- 20 Y. Mu, F. Ding and H. Lu, Strain-induced metal-semimetal transition of  $\text{BeB}_2$  monolayer, *RSC Adv.*, 2015, **5**, 11392–11396.



21 C. Wang, Q. Xia, Y. Nie, M. Rahman and G. Guo, Strain engineering band gap, effective mass and anisotropic Dirac-like cone in monolayer arsenene, *AIP Adv.*, 2016, **6**, 035204.

22 K. Zhang, M. Yan, H. Zhang, H. Huang, M. Arita, Z. Sun, W. Duan, Y. Wu and S. Zhou, Experimental evidence for type-II Dirac semimetal in PtSe<sub>2</sub>, *Phys. Rev. B*, 2017, **96**, 125102.

23 J. Kim, S. S. Baik, S. H. Ryu, Y. Sohn, S. Park, B.-G. Park, J. Denlinger, Y. Yi, H. J. Choi and K. S. Kim, Observation of tunable band gap and anisotropic Dirac semimetal state in black phosphorus, *Science*, 2015, **349**, 723–726.

24 H. Zhang, Y. Xie, Z. Zhang, C. Zhong, Y. Li, Z. Chen and Y. Chen, Dirac Nodal Lines and Tilted Semi-Dirac Cones Coexisting in a Striped Boron Sheet, *J. Phys. Chem. Lett.*, 2017, **8**, 1707–1713.

25 Z. Liu, J. Liu and J. Zhao, YN<sub>2</sub> monolayer: Novel p-state Dirac half metal for high-speed spintronics, *Nano Res.*, 2017, **10**, 1972–1979.

26 L. Wang, I. Gutiérrez-Lezama, C. Barreteau, N. Ubrig, E. Giannini and A. F. Morpurgo, Tuning magnetotransport in a compensated semimetal at the atomic scale, *Nat. Commun.*, 2015, **6**, 1–7.

27 Y. Wang, E. Liu, H. Liu, Y. Pan, L. Zhang, J. Zeng, Y. Fu, M. Wang, K. Xu, Z. Huang, Z. Wang, H.-Z. Lu, D. Xing, B. Wang, X. Wan and F. Miao, Gate-tunable negative longitudinal magnetoresistance in the predicted type-II Weyl semimetal WTe<sub>2</sub>, *Nat. Commun.*, 2016, **7**, 1–6.

28 N. D. Drummond, V. Zólyomi and V. I. Fal'ko, Electrically tunable band gap in silicene, *Phys. Rev. B: Condens. Matter Mater. Phys.*, 2012, **85**, 075423.

29 W. J. Yu, L. Liao, S. H. Chae, Y. H. Lee and X. Duan, Toward Tunable Band Gap and Tunable Dirac Point in Bilayer Graphene with Molecular Doping, *Nano Lett.*, 2011, **11**, 4759–4763.

30 S. Zhang, Y. Zhong, Y. Li, Z. Chen and H. Zeng, Atomically Thin Arsenene and Antimonene: Semimetal–Semiconductor and Indirect–Direct Band-Gap Transitions, *Angew. Chem.*, 2015, **127**, 3155–3158.

31 Z. Ni, Q. Liu, K. Tang, J. Zheng, J. Zhou, R. Qin, Z. Gao, D. Yu and J. Lu, Tunable Bandgap in Silicene and Germanene, *Nano Lett.*, 2012, **12**, 113–118.

32 M. Bernardi, M. Palummo and J. C. Grossman, Optoelectronic Properties in Monolayers of Hybridized Graphene and Hexagonal Boron Nitride, *Phys. Rev. Lett.*, 2012, **108**, 226805.

33 H. Liu, Z. Huang, C. He, Y. Wu, L. Xue, C. Tang, X. Qi and J. Zhong, Strain engineering the structures and electronic properties of Janus monolayer transition-metal dichalcogenides, *J. Appl. Phys.*, 2018, **125**, 082516.

34 R. Chaurasiya, A. Dixit and R. Pandey, Strain-driven thermodynamic stability and electronic transitions in ZnX (X = O, S, Se, and Te) monolayers, *J. Appl. Phys.*, 2019, **125**, 082540.

35 E. M. D. Siriwardane and D. Çakir, Strain engineering of electronic and magnetic properties of double-transition metal ferromagnetic semiconductor MXenes, *J. Appl. Phys.*, 2019, **125**, 082527.

36 M. Shi, P. Mo, J. Lu and J. Liu, Strain-enhanced electron mobility and mobility anisotropy in a two-dimensional vanadium diselenide monolayer, *J. Appl. Phys.*, 2019, **126**, 044305.

37 G. Kresse and J. Hafner, *Ab initio* molecular dynamics for liquid metals, *Phys. Rev. B: Condens. Matter Mater. Phys.*, 1993, **47**, 558–561.

38 G. Kresse and J. Furthmüller, Efficient iterative schemes for *ab initio* total-energy calculations using a plane-wave basis set, *Phys. Rev. B: Condens. Matter Mater. Phys.*, 1996, **54**, 11169–11186.

39 G. Kresse and D. Joubert, From ultrasoft pseudopotentials to the projector augmented-wave method, *Phys. Rev. B: Condens. Matter Mater. Phys.*, 1999, **59**, 1758–1775.

40 H. J. Monkhorst, Special points for Brillouin-zone integrations, *Phys. Rev. B: Solid State*, 1976, **13**, 5188–5192.

41 M. Gajdoš, K. Hummer, G. Kresse, J. Furthmüller and F. Bechstedt, Linear optical properties in the projector-augmented wave methodology, *Phys. Rev. B: Condens. Matter Mater. Phys.*, 2006, **73**, 045112.

42 K. S. Novoselov, A. K. Geim, S. V. Morozov, D. A. Jiang, Y. Zhang, S. V. Dubonos, I. V. Grigorieva and A. A. Firsov, Electric field effect in atomically thin carbon films, *Science*, 2004, **306**, 666–669.

43 D. Singh, S. Kansara, S. K. Gupta and Y. Sonvane, Single layer of carbon phosphide as an efficient material for optoelectronic devices, *J. Mater. Sci.*, 2018, **53**, 8314–8327.

44 Y. Li, Y. Liao, P. v. R. Schleyer and Z. Chen, Al<sub>2</sub>C monolayer: the planar tetracoordinate carbon global minimum, *Nanoscale*, 2014, **6**, 10784–10791.

45 A. Fleurence, R. Friedlein, T. Ozaki, H. Kawai, Y. Wang and Y. Yamada-Takamura, Experimental Evidence for Epitaxial Silicene on Diboride Thin Films, *Phys. Rev. Lett.*, 2012, **108**, 245501.

46 S. Kansara, S. K. Gupta, Y. Sonvane, T. Hussain and R. Ahuja, Theoretical investigation of metallic nanolayers for charge-storage applications, *ACS Appl. Energy Mater.*, 2018, **1**, 3428–3433.

47 S. Kansara, J. Shah, Y. Sonvane and S. K. Gupta, Conjugation of biomolecules onto antimonene surface for biomedical prospects: A DFT study, *Chem. Phys. Lett.*, 2019, **715**, 115–122.

48 K. Funada, A. Yamakage, N. Yamashina and H. Kageyama, Spin–Orbit-Coupling-Induced Type-I/type-II Dirac Nodal-Line Metal in Nonsymmorphic CaSb<sub>2</sub>, *J. Phys. Soc. Jpn.*, 2019, **88**, 044711.

49 X. Han, C. Liu, J. Sun, A. D. Sendek and W. Yang, Density functional theory calculations for evaluation of phosphorene as a potential anode material for magnesium batteries, *RSC Adv.*, 2018, **8**, 7196–7204.

50 J. Lee, S.-C. Lee, C. S. Hwang and J.-H. Choi, Thermodynamic stability of various phases of zinc tin oxides from *ab initio* calculations, *J. Mater. Chem. C*, 2013, **1**, 6364–6374.



51 F. Corsetti, P. Matthews and E. Artacho, Structural and configurational properties of nanoconfined monolayer ice from first principles, *Sci. Rep.*, 2016, **6**, 18651.

52 K. S. Novoselov, K. S. Novoselov, A. K. Geim, S. V. Morozov, D. Jiang, Y. Zhang, S. V. Dubonos, I. V. Grigorieva and A. A. Firsov, *Science*, 2004, **306**, 666.

53 X.-H. Peng, A. Alizadeh, S. K. Kumar and S. K. Nayak, *Ab initio* study of size and strain effects on the electronic properties of Si nanowires, *Int. J. Appl. Mech. Eng.*, 2009, **1**, 483–499.

54 S. Kansara, P. D. Bhuyan, Y. Sonvane and S. K. Gupta, Two-dimensional silicon phosphide: low effective mass and direct band gap for future devices applications, *J. Mater. Sci.*, 2019, **54**, 11878–11888.

55 L. Van Hove, The Occurrence of Singularities in the Elastic Frequency Distribution of a Crystal, *Phys. Rev.*, 1953, **89**, 1189–1193.

56 I. M. Baker, in *Springer Handbook of Electronic and Photonic Materials*, ed. S. Kasap and P. Capper, Springer International Publishing, Cham, 2017, p. 1.

